
Article:
Moon, DR, Ingham, T, Whalley, LK orcid.org/0000-0002-4486-9029 et al. (3 more authors) (2019) Production of HO_2 and OH radicals from near-UV irradiated airborne TiO_2 nanoparticles. Physical Chemistry Chemical Physics, 21 (5). pp. 2201-2824. ISSN 1463-9076

https://doi.org/10.1039/C8CP06889E

Production of HO_2 and OH radicals from near-UV irradiated airborne TiO_2 nanoparticles

D. R. Moon[1], T. Ingham[1,2], L. K. Whalley[1,2], P. W. Seakins[1,2], M. T. Baeza-Romero[3], D. E. Heard[1,2*]

[1] School of Chemistry, University of Leeds, Leeds, LS2 9JT, UK

[2] National Centre for Atmospheric Science, School of Chemistry, University of Leeds, Leeds, LS2 9JT, UK

[3] Escuela de Ingeniería Industrial, Universidad de Castilla-La Mancha, 45071, Toledo, Spain

* Corresponding author. Email: d.e.heard@leeds.ac.uk

Abstract

The production of gas-phase hydroperoxyl radicals, HO_2, is observed directly from sub-micron airborne TiO_2 nanoparticles irradiated by 300 – 400 nm radiation. The rate of HO_2 production as a function of O_2 pressure follows Langmuir isotherm behaviour suggesting O_2 is involved in the production of HO_2 following its adsorption onto the surface of the TiO_2 aerosol. Reduction of adsorbed O_2 by photogenerated electrons is likely to be the initial step followed by reaction with a proton produced via oxidation of adsorbed water with a photogenerated hole. The rate of HO_2 production decreased significantly over the range of relative humidities between 8.7 and 36.9 %, suggesting competitive adsorption of water vapour inhibits HO_2 production. From the data, the adsorption equilibrium constants were calculated to be: $K_{O2} = 0.27 \pm 0.02$ Pa^{-1} and $K_{H2O} = 2.16 \pm 0.12$ Pa^{-1} for RH = 8.7%, decreasing to $K_{O2} = 0.18 \pm 0.01$ Pa^{-1} and $K_{H2O} = 1.33 \pm 0.04$ Pa^{-1} at RH = 22.1%. The increased coverage of H_2O onto the TiO_2 aerosol surface may inhibit HO_2 production by decreasing the effective surface area of the TiO_2 particle and lowering the binding energy of O_2 on the aerosol surface, hence shortening its desorption lifetime. The maximum yield (i.e. when $[O_2]$ is projected to atmospherically relevant levels) for production of gas-phase HO_2, normalised for surface area and light intensity, was found to be $k'_{prod} = (3.64 \pm 0.04) \times 10^{-3}$ HO_2 molecule $photon^{-1}$ at a RH of 8.7% for the 80% anatase and 20% rutile formulation of TiO_2 used here. This yield decreased to $k'_{prod} = (1.97 \pm 0.03) \times 10^{-3}$ molecule $photon^{-1}$ as the RH was increased to 22.1%. Using this value, the rate of production of HO_2 from TiO_2 surfaces under atmospheric conditions was estimated to be in the range $5\times10^4 – 1\times10^6$ molecule $cm^{-3}s^{-1}$ using observed surface areas of mineral dust at Cape Verde, and assuming a TiO_2 fraction of 4.5%. For the largest loadings of dust in the troposphere, the rate of this novel heterogeneous production mechanism begins to approach that of HO_2 production from the gas-phase reaction of OH with CO in unpolluted regions. The production of gas-phase OH radicals could only be observed conclusively at

high aerosol surface areas, and was attributed to the decomposition of H_2O_2 at the surface by photogenerated electrons.

1. Introduction

The photocatalytic properties of TiO_2 are widely known [1, 2] and have been exploited in many applications such as water and air purification and self-cleaning materials. [3] TiO_2 is a semiconductor material and when illuminated with UV light an electron (e^-) is promoted from its valance band into its conduction band also creating a hole (h^+) (R1). The magnitude of the band gap for TiO_2 nanoparticles is ~ 3.2 eV, so there is a wavelength threshold of $\lambda < 388$ nm for TiO_2 to become electronically conductive. [4] The e^- and h^+ pair can migrate to the crystal surface and subsequently oxidise and reduce adsorbed donor and acceptor molecules, respectively. [5] One reaction of interest is the oxidation of water by h^+ to produce highly reactive hydroxyl radicals (OH, R2) on the TiO_2 surface. [6] Other reactive oxygenated species (ROS), such as the hydroperoxyl radical (HO_2), hydrogen peroxide (H_2O_2) and singlet oxygen ($O_2(^1\Delta)$, R3-R10), can also be formed on the surface of TiO_2 materials. The detailed reaction mechanism for the formation of these ROS on the surface of TiO_2 is not well understood, however it is believed to be as follows [6]:

$$TiO_2 + h\nu\ (\lambda < 388\ \text{nm}) \rightarrow TiO_2 + h^+ + e^- \quad \text{(R1)}$$

$$h^+ + H_2O \rightarrow OH + H^+ \quad \text{(R2)}$$

$$O_2 + H^+ + e^- \rightarrow HO_2 \quad \text{(R3)}$$

$$2OH \rightarrow H_2O_2 \quad \text{(R4)}$$

$$HO_2 + e^- + H^+ \rightarrow H_2O_2 \quad \text{(R5)}$$

$$2HO_2 \rightarrow H_2O_2 + O_2 \quad \text{(R6)}$$

$$O_2 + e^- \rightarrow O_2^- \quad \text{(R7)}$$

$$O_2^- + h^+ \rightarrow O_2\,(^1\Delta) \quad \text{(R8)}$$

$$H_2O_2 + O_2^- \rightarrow OH + OH^- + O_2 \quad \text{(R9)}$$

$$OH + HO_2 \rightarrow H_2O_2 + \tfrac{1}{2}\,O_2 \quad \text{(R10)}$$

ROS formed on the surface of the TiO_2 catalyst can react with and degrade adsorbed organic compounds making it ideal for air and water purification applications. However, some laboratory studies have shown that some ROS can also desorb from the surface of TiO_2 materials into the gas phase. Lee and Choi [7] observed the degradation of soot particles that came within close proximity, but not into direct

contact, with an illuminated substrate partially covered with TiO_2. Tatsuma et al. [8] saw the degradation of organic films placed adjacent (up to 2.2 mm) from a TiO_2 film in the presence of light and air. Both experiments indicate possible OH emissions from the surface. Murakami et al. [9] conducted the first study that directly observed gas phase OH radicals using low pressure laser induced florescence up to 8 mm from illuminated TiO_2 powders. They demonstrated that OH was produced from photocatalytic activity on the surface of the TiO_2 powder through studies using deuterated water vapour, and observed a decrease in OH signal as calcination temperatures of TiO_2 powders were increased. Vincent et al. [10] and Thiebaud et al. [11] demonstrated experimentally the formation of OH radicals and H_2O_2 molecules in the gas phase upon irradiation of TiO_2 surface in the presence of H_2O. HO_2 emissions from irradiated TiO_2 surfaces in the presence of gas phase H_2O_2 at low pressures (50 and 200 Torr) were first observed by Bahrini et al. [6] In that study HO_2 was detected up to 44 mm away from the TiO_2 surface using Cavity Ring Down Spectroscopy (cw-CDRS) which directly observed the decomposition of H_2O_2 and production of HO_2 simultaneously. Bahrini et al. [6] showed that significant concentrations of H_2O_2 (1.2 $\times 10^{14}$ molecule cm^{-3}) decomposed over 140 s until a steady state concentration was reached. In one example, it was demonstrated that 6.9×10^{11} molecule cm^{-3} of HO_2 was generated in this way. It was concluded that gas phase HO_2 was produced via the decomposition of H_2O_2 by irradiated TiO_2, however the mechanism for the formation of HO_2 was unclear. This study was taken further by Yi et al. [4] who showed that gas phase HO_2 was only produced if H_2O_2 was also present within their system and that using either N_2 or O_2 as carrier gas made little difference in gas phase HO_2 concentrations. This suggests that HO_2 was created via H_2O_2 decomposition and not from photocatalytic reduction of O_2 and that H_2O_2 serves as the electron acceptor as well as an electron donor (R11 – 12). Yi et al. also showed that different polymorphs of TiO_2, such as anatase and rutile, perform very differently with some showing rapid degradation of H_2O_2 but little HO_2 emissions and others with slower degradation but with higher emissions of HO_2. Through studies with e^- and h^+ scavengers it was shown that H_2O_2 decomposition is initiated by reaction with e^- (R11) or h^+ (R12) or OH (R13), produced via R2.

$$H_2O_2 + e^- \rightarrow OH + OH^- \qquad \text{(R11)}$$

$$H_2O_2 + h^+ \rightarrow HO_2 + H^+ \qquad \text{(R12)}$$

$$H_2O_2 + OH \rightarrow HO_2 + H_2O \qquad \text{(R13)}$$

This study reports the first direct observation of HO_2 and OH emissions when airborne TiO_2 nanoparticles are irradiated with UVA light (320 to 400 nm) in the presence of water vapour and oxygen alone (i.e. with no added H_2O_2) within an aerosol flow tube equipped with a highly sensitive laser induced fluorescence (LIF) detector for OH and HO_2 (limit of detection ~ 1×10^6 molecule cm^{-3}).

2. Experimental

2.1 Overview

Figure 1 presents a schematic diagram of the apparatus, with all experiments undertaken at room temperature (293 ± 3 K).

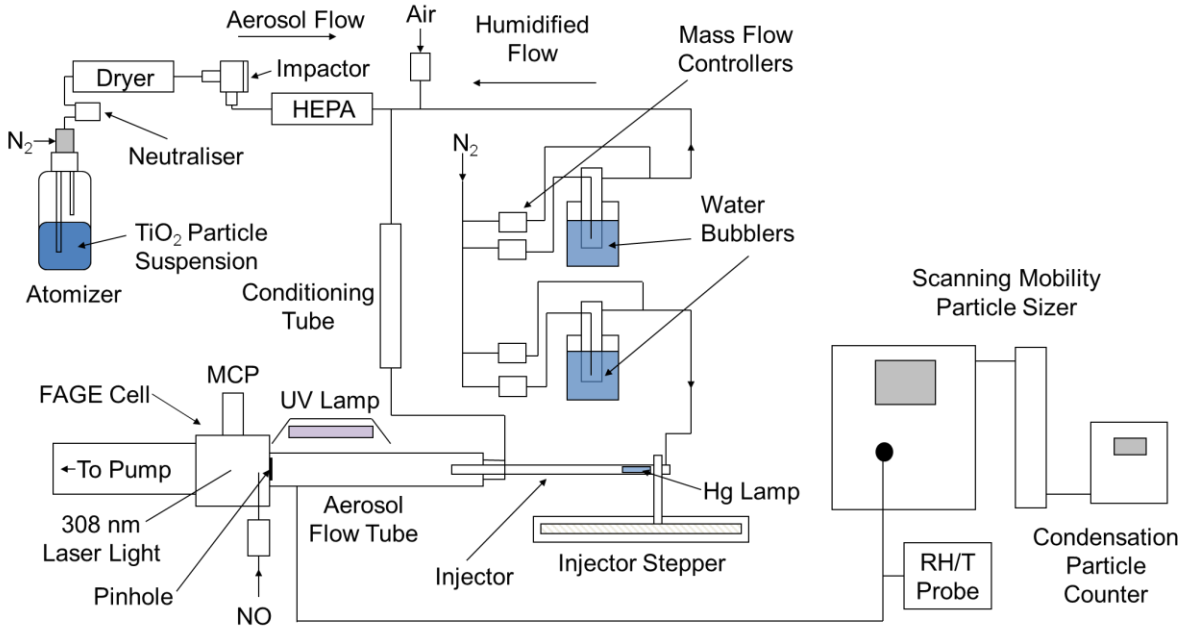

Figure 1. Schematic diagram of the aerosol flow tube experiment. MCP: Multi-Channel Plate photomultiplier, HEPA: high-efficiency particulate air filter, FAGE: fluorescence assay by gas expansion, RH/T: Relative Humidity/Temperature.

A detailed description of the apparatus, which has been used in a slightly different configuration for uptake studies of HO_2 onto a variety of sub-micron aerosols, is provided elsewhere. [12] In summary, a humidified flow of TiO_2 aerosols was introduced within a laminar aerosol flow tube reactor made from borosilicate glass (107 cm length, 5.9 cm I.D.) held at atmospheric pressure. The TiO_2 aerosols were irradiated with a UV lamp (see section 2.2) placed 5 cm above the aerosol flow tube. The HO_2 signal was then measured at the end of the aerosol flow tube using a laser-induced fluorescence at low pressure, a technique known as Fluorescence Assay by Gas Expansion (FAGE, see section 2.4), after chemical conversion by its reaction with NO to OH. [13] The size distribution of TiO_2 aerosols within the aerosol flow tube was measured using a Scanning Mobility Particle Sizer (SMPS, see section 2.3) from a flow sampled from the exhaust of the aerosol flow tube. All gas flows within the experiment were controlled using mass flow controllers (Brookes and MKS). The RH and temperature of the flow was measured using a calibrated probe (Rotronics Hygroclip2, accuracy ± 0.8% RH and ± 0.1 K) in the exhaust of the aerosol flow tube.

2.2 Aerosol Irradiation

The aerosol flow tube was illuminated with a UV lamp located adjacent to the FAGE cell and approximately 5 cm above the aerosol flow tube. Two UV lamps were used in this study; a 15 W UVA bench lamp (which has two 420 mm length fluorescent tubes, UVP, XX-15) and an 8 W UVA lamp (1 × 8 W 300 mm length fluorescent tube, Eterna, LFT58WH). The 15 W UVA lamp was used in all studies unless otherwise stated. The absolute lamp fluxes of the lamps as a function of wavelength were measured using a calibrated spectral radiometer (Ocean Optics QE500) as is shown in Figure 2. These fluxes were measured outside the aerosol flow tube since it was not possible to fit the integrating dome of the spectral radiometer within the aerosol flow tube due to space constraints. Both the aerosol flow tube and the halocarbon wax film, which was applied to the walls of the aerosol flow tube to reduce HO_2 wall losses, attenuates light entering the aerosol flow tube. An experiment was conducted where the spectral output of the 8 W lamp whilst it was placed inside the aerosol flow tube was measured with the integrating dome of the spectral radiometer placed outside the aerosol flow tube and positioned where the UV lamps are usually placed (with the same distance from lamp to integrating dome). This experiment showed that the total flux of UVA photons from the 8W lamp (integrated between 250 and 388 nm) placed inside the aerosol flow tube was 16 times lower than when the flux was measured with the lamp outside the aerosol flow tube (as shown in Figure 2) for the same lamp to integrating dome distance. Hence the light flux inside of the aerosol flow tube with the lamp placed outside is assumed to be 16 times smaller than shown in Figure 2, although it is realised there are considerable uncertainties, for example the circular nature of the flow-tube may create a heterogeneous light field within the aerosol flow tube and there is an opposite lensing effect for the two cases. The attenuation factor from the tube/wax was found to be approximately constant with wavelength across the spectral output of the 8 W lamp, and hence it was assumed for the 15 W lamp (which would not fit within the flow tube) that the flux inside the flow tube would scale in a similar manner and be 16 times lower than shown in Figure 2.

Figure 2 also compares the spectral variation of the flux of the lamps to a typical actinic flux spectrum measured at a mid-latitude coastal site in the UK in summer. The amount of light with $\lambda < 388$ nm (threshold for promotion of electron to the TiO_2 conduction band) from the 8W lamp entering the flow tube was ~ 7 times smaller than that from typical actinic fluxes experienced within the troposphere and ~ 5 times smaller than fluxes from the 15 W lamp. The amount of such light emitted from the 15 W lamp entering the flow tube was comparable to typical actinic fluxes, which are 40% greater. There are also notable differences in the emission spectra of the two lamps. The average wavelength emitted from the 15 W lamp (340 nm) is smaller than the 8W lamp (365 nm) and the 15 W lamp emits a broader

range of wavelengths in the ultraviolet region (275 – 400 nm) compared to the 8 W lamp (325 – 400 nm).

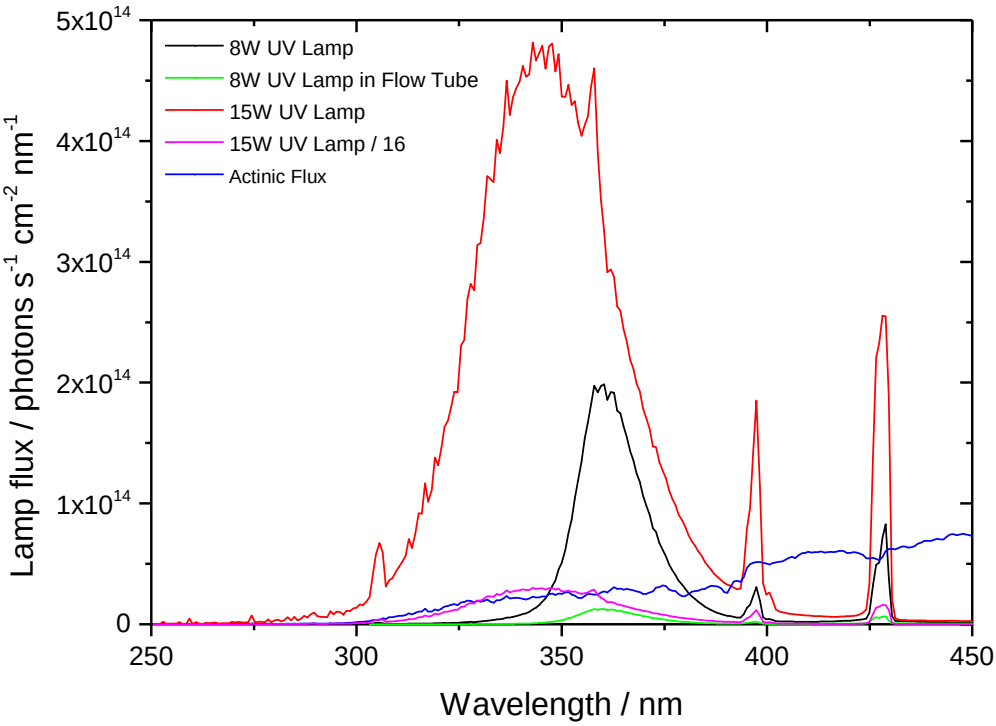

Figure 2. UVA emission spectra for the 8 W UVA lamp inside (green line) and outside (black line) the aerosol flow tube and the 15 W UVA lamp inside (purple line) and outside (red line) the aerosol flow tube, in all cases with the spectral radiometer integrating dome outside the flow tube. In all cases the distance from the lamp to the spectral radiometer integrating dome was constant. The actinic flux (blue line) measured at the Weybourne Atmospheric Observatory (Norfolk Coast, UK, 52º57'N, 1º07'E) on the 1st July 2015 is shown for comparison.

2.3 Aerosol Generation and Detection

A suspension of TiO_2 nanoparticles (Aldrich Chemistry 718467, 99.5% Degussa, 5 g in 500 ml of Milli-Q water) was placed in a commercial atomizer (TSI 3076) which was in turn connected to compressed nitrogen which produced a 3.5 L min^{-1} flow entrained with TiO_2 particles, of which 1.5 L min^{-1} was introduced into the apparatus (referred to as the aerosol flow) and the rest left the apparatus through an exhaust. The nanoparticles are composed of 80% anatase and 20% rutile, polymorphs of TiO_2. Similar formulations of TiO_2, such as Degussa P25 (75% anatase and 25% rutile), are widely used in laboratory studies [2], and have been shown to have enhanced photocatalytic activity as electrons can rapidly transfer from the rutile to anatase crystallites which results in photoactivity occurring at visible wavelengths and creates enhanced catalytic activity at the rutile-anatase interface. [14] The aerosol flow was then passed through a neutraliser to reduce static wall losses, a diffusion drier and an impactor (TSI 1034900) to

ensure larger aerosols beyond the detection range of the SMPS (~ 750 nm) do not enter the aerosol flow tube. A high-efficiency particulate air (HEPA, PALL Life Sciences) filter situated within a by-pass loop was used to control the number concentration of particles entering the aerosol flow tube. The aerosol flow was then mixed with a humidified flow of nitrogen to control the RH within the system. The RH of the humidified flow was altered by changing the ratio of dry nitrogen and nitrogen passed through a water bubbler. Oxygen was introduced into the system via zero air (BOC UN1002, 20% O_2 and 80% N_2) before the aerosol and humidified flow enters the conditioning tube and controlled using a calibrated mass flow controller (Alicat Scientific). This flow was then passed through a conditioning tube (residence time ~ 5 s) before entering the aerosol flow tube to allow time for adequate mixing of the three flows and water vapour adsorption onto the surface of the TiO_2 particles to equilibrate at the given RH. The combined flow rate through the aerosol flow tube was 5.3 L min^{-1}.

The aerosol size distribution and number concentration was measured over a period of 180 s once during each measurement using a Scanning Mobility Particle Sizer (SMPS, TSI 3081) and condensation particle counter (CPC, TSI 3775), from which the total surface area and average radius of particles can be calculated, assuming that particles are spherical. Scanning Electron Microscope images of the TiO_2 particles used within the experiments showed that these particles are indeed spherical. [12] Measurements of the size distribution of the TiO_2 aerosols were made at the beginning and end of the aerosol flow tube which showed that there only a small loss of aerosols during transit of the flow tube (< 5%).

2.4 HO_2 and OH Radical Detection

OH and HO_2 (HO_x) radicals were detected by Fluorescence Assay by Gas Expansion (FAGE, detection limit 10^6 molecule cm^{-3}). [15] HO_x radicals entered the FAGE cell placed at the end of the flow tube through a 0.7 mm diameter pinhole. In order to detect HO_2, it was chemically converted to OH by injecting 50 sccm of NO (BOC, 99.5 %) into the resulting jet on the low pressure side of the pinhole. The $Q_1(2)$ line of the OH ($A^2\Sigma^+ - X^2\Pi_i v' = 0 - v'' = 0$) transition at $\approx$ 308 nm was used to electronically excite the OH in the FAGE cell. A Nd:YAG pumped dye laser (JDSU Q201-HD Q-series, Sirah Cobra Stretch) was used to produce the required 308 nm radiation (line width $\approx$ 0.1 cm^{-1}) at a pulse repetition rate of 5 kHz. The FAGE cell was continuously evacuated using a combination of a rotary pump (Edwards, model E1M80) and a roots blower (EH1200), and was kept at 0.8–0.9 Torr, which was monitored using a capacitance monitor (Tylan General, CDC 11). The FAGE signal was calibrated using a turbulent flow tube calibration method [16] which has been developed for field measurements of OH and HO_2 radicals, meaning the LIF signal could be converted into an absolute concentration. The calibration experiment involves generating known concentrations of OH and HO_2 from photolysis of H_2O vapour in zero air in a turbulent flow tube placed immediately adjacent to the FAGE sample inlet.

2.5 Experimental Procedure and Data Analysis

At the beginning of all experiments the FAGE background measurements without the UVA lamp on were taken without and with NO injected into the FAGE cell and subtracted from the OH and HO_2 signals respectively, to correct for laser scatter and photolysis of any impurities in the NO which may form OH. The FAGE signal was averaged over 20 s (average of twenty 1 s data points, each corresponding to 5000 laser shots) for each measurement. Eight 20 s measurements were taken during each run. Measurements were made in the absence of aerosols and in the presence of aerosols. Measurements of HO_x concentrations produced from TiO_2 aerosols under varying conditions were made at different total surface area densities of TiO_2 aerosols, RH, light flux and oxygen concentration. The laser power was recorded for each measurement and used to normalise the HO_2 signal to correct for any fluctuations in laser power (< 5% during an experiment).

The HO_2 signal measured at the end of the aerosol flow tube results from several radical production and loss processes, namely wall loss (R14), aerosol uptake (R15), HO_2 self-reaction in the gas-phase (R16), production of HO_2 from aerosols which have been deposited on the walls of the aerosol flow tube (R17) and HO_2 production from airborne TiO_2 aerosol surfaces (R18). To obtain the rate coefficient k_{prod} for HO_2 production from processes occurring on airborne aerosol surfaces, reactions (R14)-(R18) were all included in a numerical model developed within the Kintecus integrator package (Windows Version 2.80). [17] The HO_2 concentration measured at the end of the flow tube after illumination for a known period of time was used as the target parameter for the model.

$$\mathrm{HO_2} \xrightarrow{k_{wall}} \text{Wall loss} \tag{R14}$$

$$\mathrm{HO_2} \xrightarrow{k_{uptake}} \text{Aerosol Uptake} \tag{R15}$$

$$\mathrm{HO_2} + \mathrm{HO_2} \xrightarrow{k_{self}} \mathrm{H_2O_2} + \mathrm{O_2} \tag{R16}$$

$$\text{Wall} + h\nu \xrightarrow{k_{prod\,wall}} \mathrm{HO_2} \tag{R17}$$

$$\mathrm{TiO_2}\ \text{aerosol} + h\nu \xrightarrow{k_{prod}} \mathrm{HO_2} \tag{R18}$$

The HO_2 wall loss rate coefficient (k_{wall}) used in the model was determined at the beginning and end of each experiment using a methodology previously described [12] in which a sliding injector emitting HO_2 was translated down the flow tube in the absence of aerosols (but after the walls have been conditioned in the presence of aerosols). Wall losses increased as RH was increased during experiments. The HO_2 concentration as a function of time along the flow tube when determining k_{wall} (as k_{self} is negligible in at the HO_2 concentrations of these experiments) can be expressed as:

$$\ln[\mathrm{HO_2}]_t = \ln[\mathrm{HO_2}]_0 - k_{wall}t \tag{E2}$$

where $[HO_2]_t$ and $[HO_2]_0$ are concentrations of HO_2 at time t and t = 0 (i.e. $[HO_2]$ at initial injector position) respectively, and k_{wall} is the observed pseudo-first-order rate coefficient for HO_2 wall losses. This rate constant was determined in independent experiments where HO_2 was generated in the injector as in previous work [9] in the absence of aerosols. Similar HO_2 concentrations were used in these experiments and in HO_2 generation experiments.

The aerosol loss rate coefficient, $k_{aerosol\ loss}$, was calculated using E3:

$$k_{aerosol\ loss} = 0.25\, S_a \omega_{\mathrm{HO_2}} \gamma(\mathrm{HO_2}) \tag{E3}$$

where $\gamma(HO_2)$ is the reactive uptake coefficient of HO_2 onto TiO_2, which was previously measured in this laboratory in the absence of light [12], S_a is the surface area density of TiO_2 aerosols and w_{HO2} is the molecular speed of HO_2. The self-reaction of HO_2 (R16) in the gas-phase contributes a negligible HO_2 loss pathway (~ 0.01 %) at the HO_2 concentrations used. The production of HO_2 from the surfaces of the flow tube walls and TiO_2 aerosols was characterised in Kintecus using equations (E4) and (E5), respectively:

$$\frac{d[\mathrm{HO_2}]}{dt} = k_{wall\ prod}[\mathrm{Wall}] \tag{E4}$$

$$\frac{d[\mathrm{HO_2}]}{dt} = k_{prod} S_a \tag{E5}$$

where [Wall] is the surface area concentration ($cm^2\ cm^{-3}$) of the illuminated walls of the aerosol flow tube (i.e. surface area of the interior walls of the aerosol flow tube divided by the internal volume of aerosol flow tube) and S_a is the surface area density of the TiO_2 aerosols, determined by the SMPS. Using [Wall], S_a, k_{self}, k_{wall}, and $k_{aerosol\ loss}$ as constraints, which are all known for a given experiment, the Kintecus model was used to calculate $[HO_2]$ at the appropriate illumination time, which is also known for a given lamp. With the lamp illuminating the flow tube, but in the absence of aerosols ($S_a = 0$), the value of $k_{prod\ wall}$ within Kintecus was optimised to give the best fit with measured $[HO_2]$ at the end of the flow-tube after the known illumination time. Using this value of $k_{wall\ prod}$, but now in the presence of aerosols at a given S_a, the value of k_{prod} was optimised within Kintecus to match $[HO_2]$ at the end of the flow tube. k_{prod} describes the rate of HO_2 production per unit surface area of TiO_2 aerosols, and is expected to depend on experimental variables such as $[O_2]$, RH and lamp radiation flux (which itself is a function of S_a). In the following section, the HO_2 concentration was measured at the end of the flow tube whilst changing a number of variables, and Kintecus was used to obtain an optimised value of k_{prod} for each set of experimental conditions.

3. Results

3.1 HO_2 production by irradiated airborne TiO_2 nanoparticles

3.1.1. Variation with aerosol surface area and lamp flux

Initial experiments were performed using a carrier gas consisting of either pure nitrogen or 5.9% O_2 in nitrogen. Figure 3 displays the concentration of HO_2 measured at the end of the aerosol flow tube (corresponding to 14 s of exposure to the lamp radiation) as a function of the surface area density of airborne TiO_2 nanoparticles, S_a. In the presence of O_2 a significant increase of gas-phase HO_2 was measured as S_a was increased, however when the carrier gas was composed of solely compressed nitrogen at similar RH no significant change was observed. These experiments suggest that the HO_2 produced was from the surfaces of irradiated airborne TiO_2 nanoparticles via a photocatalytic mechanism involving adsorbed molecular oxygen. A small HO_2 signal was detected at $S_a = 0$ (i.e. when airborne TiO_2 nanoparticles were not present in the aerosol flow tube) likely associated with production from previously deposited TiO_2 nanoparticles on the walls of the aerosol flow tube and O_2 impurities in the nitrogen (estimated at ~ 100 ppm). No such HO_2 signal was observed after the aerosol flow tube had been cleaned. The small concentration of HO_2 produced from the walls at $S_a = 0$ was included within the Kintecus model using (R17) and $k_{prod\ wall}$ (E4).

Figure 3 shows that HO_2 increases as more airborne TiO_2 nanoparticles enter the system until a maximum was reached, after which adding more particles results in a decrease in the HO_2 concentration. Two processes may account for this. TiO_2 aerosols have a large refractive index (2.5 at 500 nm) [18], therefore lamp radiation entering the aerosol flow tube will be Mie scattered by the aerosols shading those aerosols below and which may result in a drop in the overall photocatalytic activity of TiO_2 aerosols, and hence the total rate of production of HO_2. Moreover, as the aerosol loading of the flow tube increases the rate of reactive heterogeneous uptake of HO_2 by TiO_2 aerosols via reaction (R15) also increases and will compete with HO_2 production.

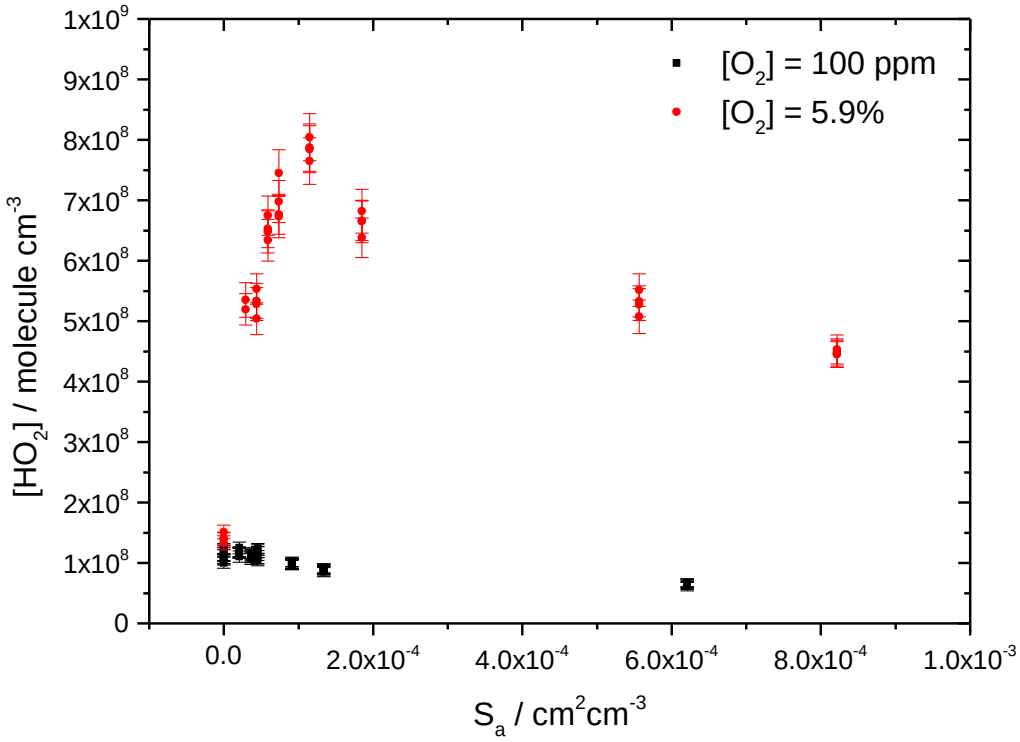

Figure 3. Gas phase HO_2 produced by airborne irradiated TiO_2 nanoparticles as a function of surface area density, S_a, with a carrier gas composed of compressed nitrogen with ~ $[O_2]$ = 100 ppm impurity (solid black squares) at RH = 24.0%, and for a 5.9 % mixture of O_2 (balance N_2) (filled red squares) at RH = 16.4%. At S_a = 0, the HO_2 is due to production at the flow tube walls. The aerosol flow tube was illuminated with the 15 W lamp. The illumination time = 14 s.

Figure 4 compares the HO_2 produced as a function of S_a when the 8 W and 15 W UVA lamps were used to illuminate the aerosol flow tube. As expected, the use of the higher-powered lamp resulted in more gas-phase HO_2 being produced, however the 15 W UVA lamp is also longer by 12 cm (40%) resulting in aerosols being irradiated for 4 s longer than with the 8 W lamp and will also account for the higher concentrations of HO_2 produced. A similar dependence of HO_2 production with varying S_a was observed.

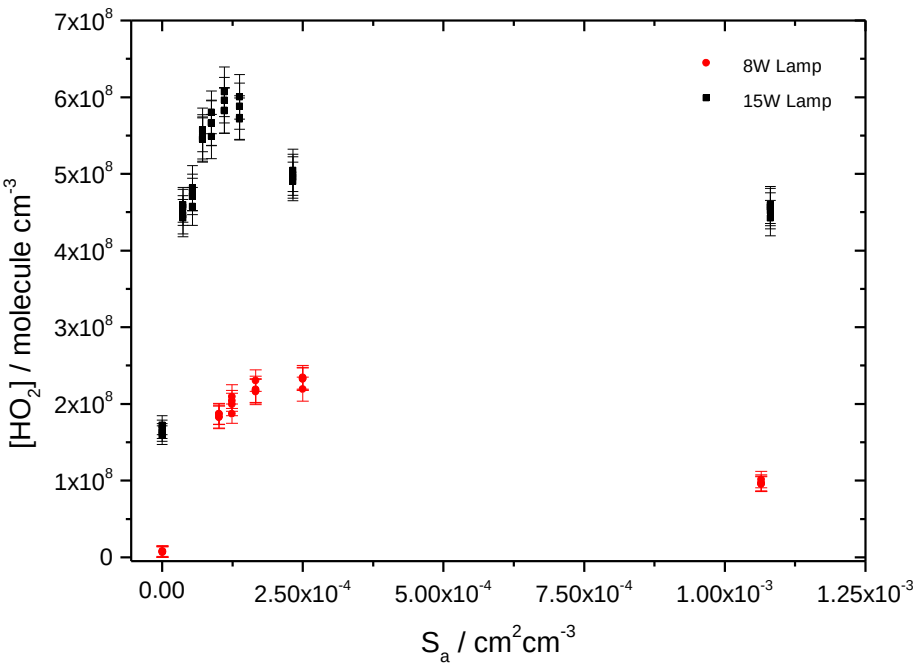

Figure 4. Gas phase HO_2 produced from airborne irradiated TiO_2 nanoparticles as function of total surface area density (S_a) at RH = 8.0% and [O_2] = 5.9% using an 8 W UVA lamp (red circles) and a 15 W UVA lamp (black squares) to illuminate the aerosol flow tube. The illumination time for 15 W lamp = 14 s and 8 W lamp = 10 s. The ratio of flux with λ < 388 nm that enters the flow tube emitted from the 8 W and 15 W lamp was 1:5.

Using the constrained model described by reactions (R14) – (R18), the optimised value of k_{prod} (the number of HO_2 molecules emitted per cm^2 of particle surface per second) was calculated to give the best fit to the measured [HO_2] at the end of the flow tube after illumination. The variation of k_{prod} as a function of S_a is shown in Figure 5 for both lamps, and shows k_{prod} decreases rapidly with S_a, which is expected given the decreasing rate of production of HO_2 with S_a seen in Figure 4. The inverse dependence of k_{prod} with S_a is consistent with aerosol light scattering reducing the photons per unit surface area interacting with the TiO_2 surface. At low S_a, k_{prod} using the 15 W lamp was significantly greater than k_{prod} using the 8 W lamp, which is expected owing to the larger light flux, although the production of HO_2 below 388 nm may also be wavelength dependent. However, as the aerosol loading within the aerosol flow tube was increased, k_{prod} using the 15 W lamp decreases ~ 3 times faster than for the 8 W lamp, suggesting light from the 15 W lamp is more affected by aerosol scattering. At high S_a, k_{prod} reaches a minimum value which is ~ 5 times larger for the 15 W lamp than the 8 W lamp, consistent with the ratio of lamp fluxes for λ < 388 nm of the two lamps entering the flow tube. As seen in Figure 2 the 15 W lamp emits UV light across a much broader range of wavelengths (275 – 400 nm) with an average wavelength of 340 nm compared to the 8 W lamp which emits across a smaller range of wavelengths (325 – 400 nm) with an average wavelength of 365 nm. As the refractive index of a

material and the Mie scattering are inversely proportional to the wavelength of light, the 15 W lamp radiation may be more efficiently scattered.

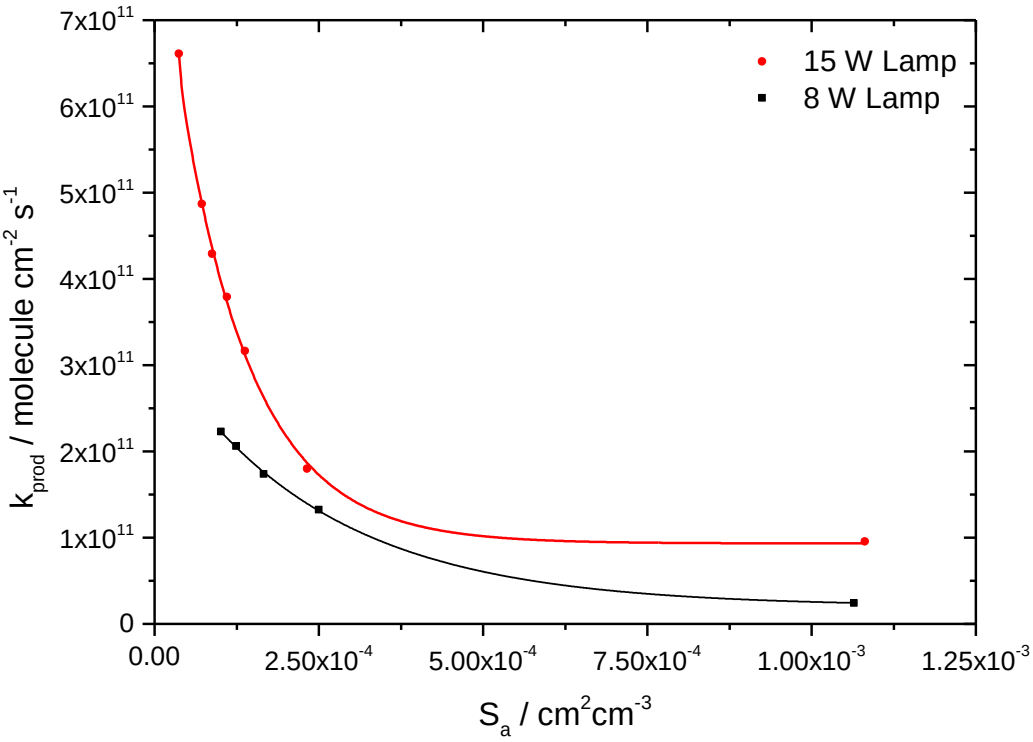

Figure 5. The variation of k_{prod} as function of total surface area density (S_a) of TiO_2 nanoparticles at RH = 8.0% and [O_2] = 5.9% using the 8 W UVA lamp (black squares) and the 15 W UVA lamp (red circles) to illuminate the aerosol flow tube. Solid lines represent exponential decays as a guide to the eye. The lamps have different fluxes (see text for details).

The value of k_{prod} depends on several factors, including the lamp flux λ < 388 nm, F, and a flux-independent rate coefficient, k'_{prod}, can be defined as $k_{prod} = F\, k'_{prod}$. Figure 6 shows that values of k'_{prod} decayed exponentially as the aerosol loading was increased in the aerosol flow tube. At the lowest value of S_a (~ 1 × 10^{-4} cm^2 cm^{-3}) and using the lamp flux appropriate for within the flow tube, the values of k'_{prod} for the 8W and 15 W lamps were determined to be 6.4 × 10^{-4} and 2.3 × 10^{-4} HO_2 molecule photon^{-1} respectively (see Figure 6), with an average value of 4.4 × 10^{-4} HO_2 molecule photon^{-1}. This shows that HO_2 production was 2.8 times more efficient when using 8 W lamp, likely due to greater levels of scattering or lesser levels of absorbance of light from the 15 W lamp. However, at the highest S_a (~ 1 × 10^{-3} cm^2 cm^{-3}) where k_{prod} reaches a minimum and scattering reaches its maximum level the values of k'_{prod} for the 8 W and 15 W were broadly consistent and determined to be (7.4 ± 0.3) × 10^{-5} and (5.9 ± 0.4) × 10^{-5} HO_2 molecule photon^{-1} respectively, with an average value of 6.7 × 10^{-5} HO_2 molecule photon^{-1}. .

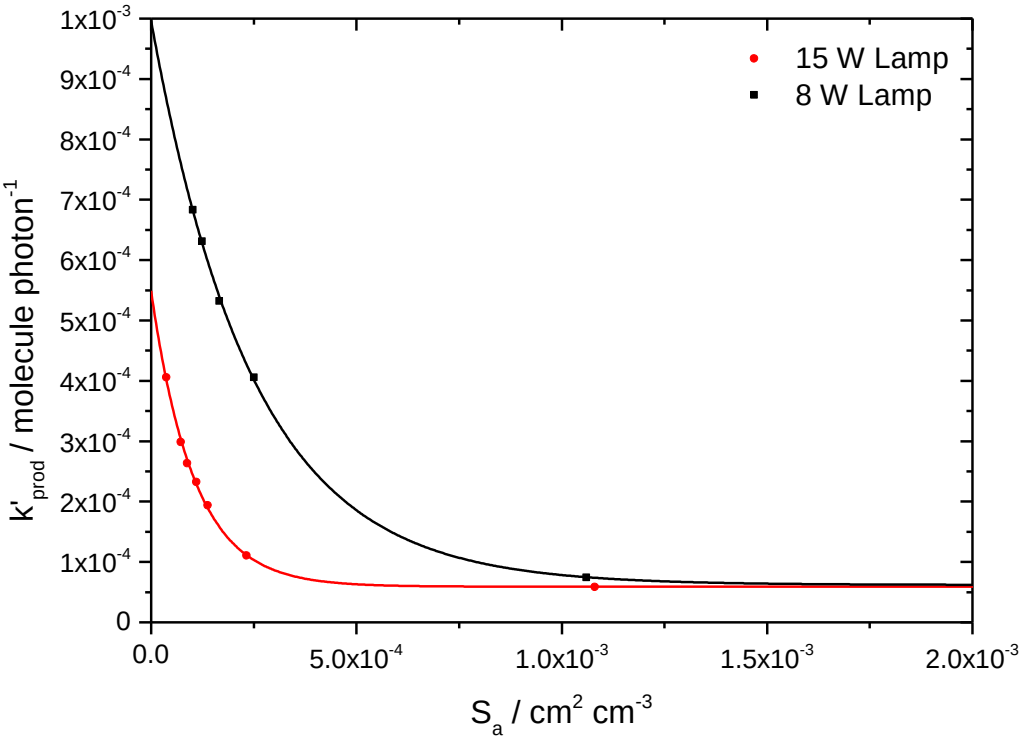

Figure 6. The variation of k'_{prod} as function of total surface area density (S_a) of TiO_2 nanoparticles at RH = 8.0% and $[O_2]$ = 5.9% using the 8 W UVA lamp (black squares) and the 15 W UVA lamp (red circles) to illuminate the aerosol flow tube. Solid lines represent exponential decays as a guide to the eye.

3.1.2. Variation with illumination time, $[O_2]$ and RH

Further experiments were conducted at low aerosol surface area densities (~ 1 – 2 × 10^{-5} cm^2 cm^{-3}) to reduce the effects Mie scattering and aerosol uptake of HO_2, and Figure 7 shows the HO_2 concentration per unit surface area measured at 4 different illumination times, which was varied by masking different lengths of the 15 W lamp, and for two different $[O_2]$. The rate of production of HO_2 appears to slow down with irradiation time (although not observed it is expected HO_2 production would reach a steady-state value at longer time) and increases with the O_2 mixing ratio. The observed slowdown of HO_2 produced is associated with wall loss and aerosol uptake.

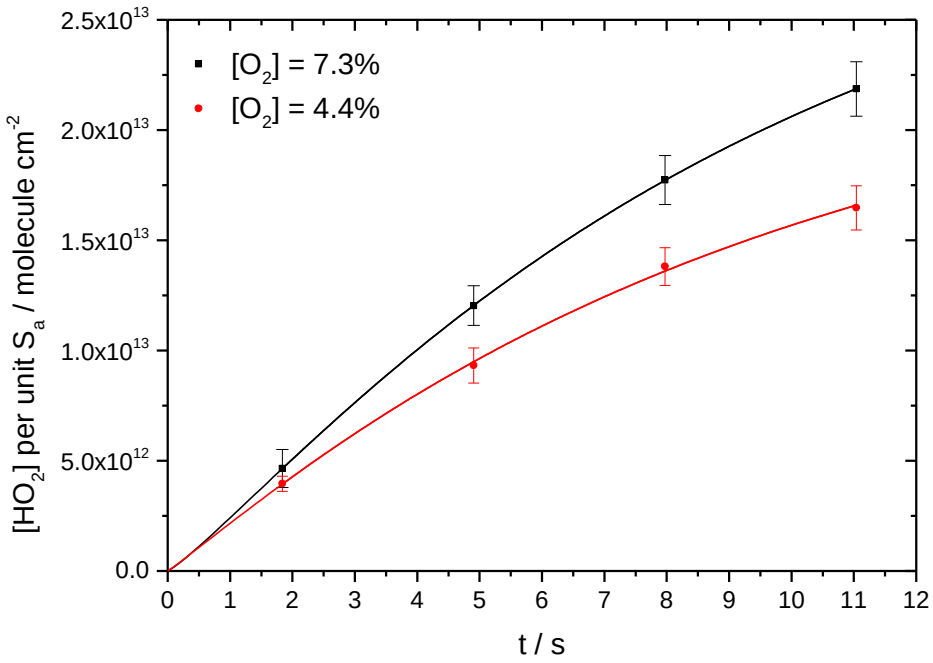

Figure 7. Time dependence of HO_2 produced by the 15 W UVA lamp at 4 illumination times for S_a = 1.6×10^{-5} cm^2 cm^{-3}, RH = 11.0% and at $[O_2]_{t=0}$ = 7.3% (black squares) and 4.4% (red circles) RH = 11.0%. The solid lines are a polynomial fit as a guide to the eye. Error bars represents 1σ of the data points taken over the 20 s averaging period.

For a fixed illumination time of 14 s (the lamp was unmasked), the dependence of $[HO_2]$ at the end of flow tube was measured as a function of $[O_2]$ over the mixing ratio range 0-8 %. Using the Kintecus model described above, k_{prod}, the rate coefficient for HO_2 production from illuminated aerosols was calculated and is shown as a function of the partial pressure, pO_2, in Figure 8 for two different RH. The relationship between k_{prod} and pO_2 in Figure 8 shows typical Langmuir adsorption behaviour, described by the reaction scheme:

$$[O_{2(g)}] \underset{k_{-1}}{\overset{k_1}{\leftrightharpoons}} [O_{2(ad)}] \xrightarrow{k_2} [HO_2] \qquad \text{(R19)}$$

with HO_2 postulated as being generated from the oxidation of adsorbed water vapour by a photogenerated hole (h^+) (R2) to form H^+, and reaction of H^+ with O_2 and a photogenerated e^- (R2 – R3).

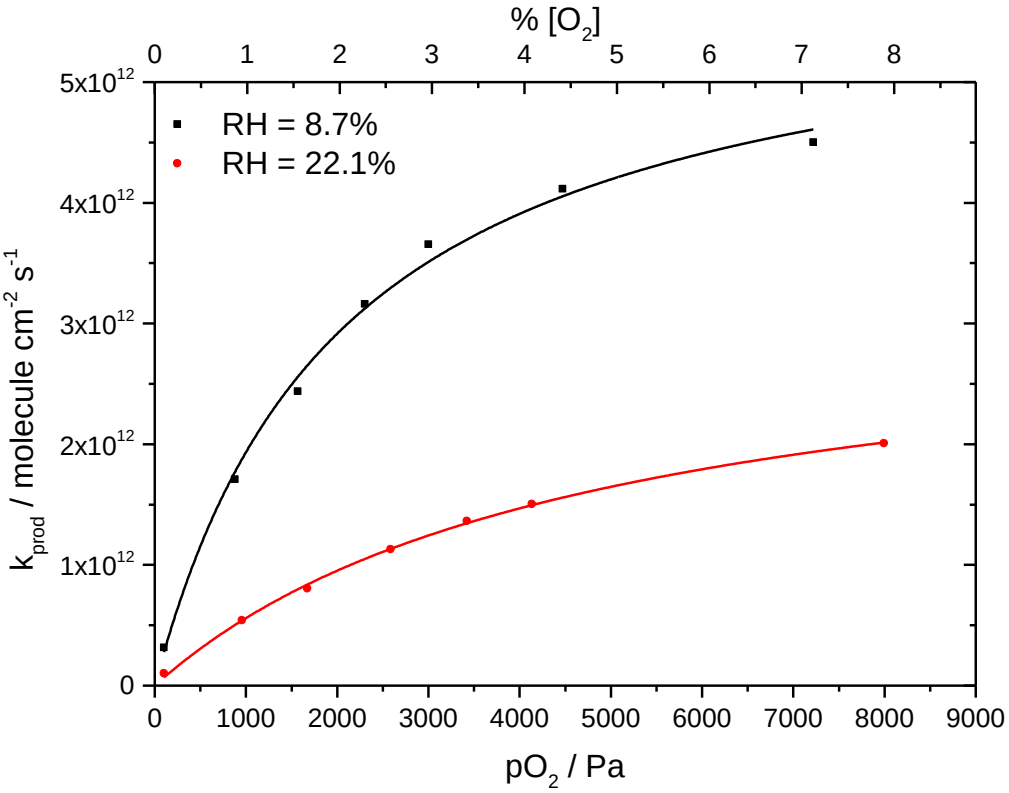

Figure 8. k_{prod}, the rate coefficient for the production of gas-phase HO_2 from irradiated airborne TiO_2 nanoparticles as a function of O_2 partial pressure and for RH = 8.7% (black squares) and 22.1% (red circles). The solid lines represent fits of the Langmuir expression equation (E7) to the data, see text for details. Light intensity λ < 388 nm = 1.63×10^{15} photons cm^{-2}.

The relationship between the rate of HO_2 formation and the amount of water vapour within the aerosol flow tube was investigated more extensively. Figure 9 shows that the concentration of HO_2 produced per unit surface area decreases significantly as the relative humidity was increased within the aerosol flow tube. As expected from Figure 8, tripling the concentration of O_2 only resulted in a modest increase in HO_2 production. Beyond a RH of ~ 40% k_{prod} appears to approach a minimum value and H_2O no longer has an inhibiting effect to HO_2 production. From FTIR studies of TiO_2 aerosols in the presence of various RH this corresponds to a H_2O surface coverage of 1.6 monolayers. [19]

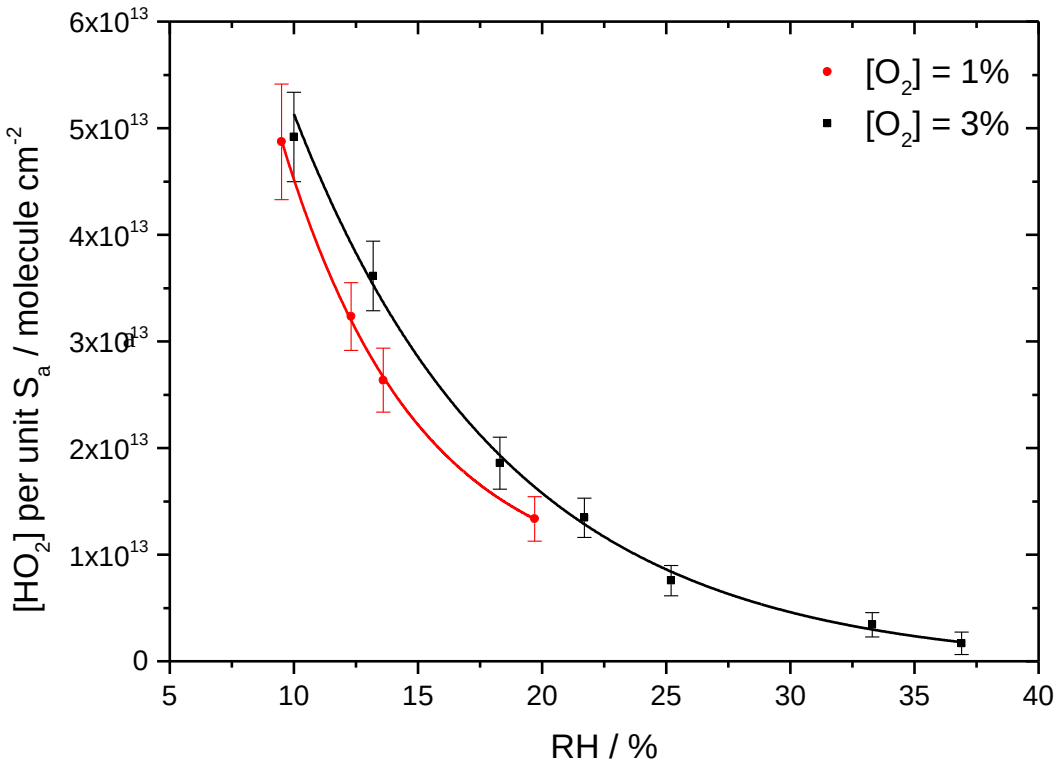

Figure 9. Gas-phase HO_2 concentration per unit of S_a for airborne TiO_2 nanoparticles at an illumination time of 14 s as a function at different RH for $[O_2]$ = 1% (red circles) and 3% (black squares). Solid lines represent exponential decay fits to experimental data as a guide to the eye. Error bars represents 1σ of the data points taken over the 20 s averaging period.

Figures 8 and 9 suggests adsorption of water vapour inhibits HO_2 production by reducing the effective surface area of the particle and therefore reducing the number of available sites on the TiO_2 particle surface that O_2 can adsorb and react on. The total concentration of active sites, $[S_0]$, is given by:

$$[S_0] = [S] + [H_2O_{(ad)}] + [O_{2(ad)}] \tag{E4}$$

where [S] is the concentration of unoccupied sites, and $[H_2O_{(ad)}]$ and $[O_{2(ad)}]$ are the density of sites inhibited or occupied by water vapour and O_2, respectively. The equilibrium constant for adsorption of O_2 or water vapour is defined by:

$$K_A = \frac{k_1}{k_{-1}} = \frac{[A_{(ad)}]}{p_A[S]} \tag{E5}$$

where k_1 and k_{-1} is the rate of adsorption and desorption respectively, A = O_2 or H_2O, p_A is the partial pressure of A and $[A_{(ad)}]$ is the concentration of A adsorbed on the surface. For Langmuir adsorption within the presence of an inhibiting species, the fractional coverage of O_2, θ_{O2}, defined as the fraction of actives sites on the TiO_2 nanoparticle surface occupied by O_2, is given by:

$$\theta_{O_2} = \frac{[O_{2(ads)}]}{[S_0]} = \frac{K_{O_2}p_{O_2}}{1+K_{O_2}p_{O_2}+K_{H_2O}p_{H_2O}} \tag{E6}$$

where K is the adsorption equilibrium constant for O_2 or H_2O vapour on TiO_2, and p is the partial pressure of O_2 or H_2O vapour. From experiments using IR spectroscopy Goodman et al. [17] showed that at RH = 8.7% and 22.1% the number of monolayers of H_2O is 0.9 and 1.2 respectively on TiO_2. Assuming reaction (R3) is the rate determining step, the rate of production of HO_2 from the TiO_2 aerosols (k_{prod}) is then given by:

$$k_{prod} = k_2\theta_{O_2} = \frac{k_{prod\,max}K_{O_2}p_{O_2}}{1+K_{O_2}p_{O_2}+K_{H_2O}p_{H_2O}} \quad \text{(E7)}$$

where $k_{prod\ max}$ is the maximum rate coefficient of production of HO_2 at high partial pressures of O_2. Figure 8 also includes a fit of E7 to the experimental data which yielded best-fit values for $k_{prod\ max}$, K_{O2} and K_{H2O}, which are summarised in Table 1.

Table 1. Parameters yielded from fitting E7 to the experimental data in Figure 8 (error = 2σ). Average $S_a = 1.5 \times 10^{-5}$ cm^2 cm^{-3}. Light intensity λ < 388 nm = 1.63×10^{15} photons cm^{-2}

Parameter	RH = 8.7%	RH = 22.1%
$k_{prod\ max}$ / molecule cm^{-2} s^{-1}	$(5.93 \pm 0.07) \times 10^{12}$	$(3.21 \pm 0.02) \times 10^{12}$
$k'_{prod\ max}$ / molecule photon^{-1}	$(3.64 \pm 0.04) \times 10^{-3}$	$(1.97 \pm 0.03) \times 10^{-3}$
K_{O2} / Pa^{-1}	0.269 ± 0.016	0.184 ± 0.004
K_{H2O} / Pa^{-1}	2.16 ± 0.12	1.33 ± 0.04

A measurement of K_{H2O} onto a TiO_2 surface has previously been conducted via a study of the photocatalytic reduction of CO_2 with H_2O. [20] However, key descripancies between the studies make the measurements incomparable; i.e., the measurements in this study were regarding surfaces of airborne Degussa TiO_2 nanoparticles, whereas that study concerned a graphene oxide-supported oxygen-rich TiO_2 hybrid, which was used to coat the walls of a flow tube. There are no previous measurements of K_{O2} on TiO_2 surfaces to our knowledge.

3.2 OH formation by irradiated airborne TiO_2 nanoparticles

OH production from irradiated TiO_2 aerosols was also investigated. The FAGE instrument operated with no added NO in the fluorescence cell did not see any OH signal from TiO_2 aerosols illuminated within the aerosol flow tube. However, this observation might be explained by OH losses to the walls of the flow tube or via reactions of OH with impurities before entering the FAGE sampling nozzle. To test this hypothesis, CO (0.5 L min^{-1}, 5% in air) was added to the carrier gas prior to the conditioning tube to rapidly scavenge any OH generated from the aerosol surface via the reaction:

$$CO + OH\ (+ O_2) \rightarrow CO_2 + HO_2 \quad \text{(R20)}$$

Any additional OH signal when CO was added would provide evidence for aerosol production of OH. In the flow tube [CO] = 1.1×10^{17} molecule cm^{-3}, giving an OH lifetime of = 5.5×10^{-5} s, during which it only moves ~ 1.4×10^{-4} cm along the flow tube, and other loss processes should not compete. Figure 10 shows that for aerosol surface areas (S_a) lower than 2×10^{-4} cm^2 cm^{-3} there was no discernible difference between HO_2 produced with and without CO present, for RH = 10 – 12%. However, for S_a > 2×10^{-4} cm^2 cm^{-3}, a noticeable difference ([OH] ~ 8×10^8 molecule cm^{-3}) was observed, providing some evidence for OH production, although the uncertainties are quite high at the largest S_a.

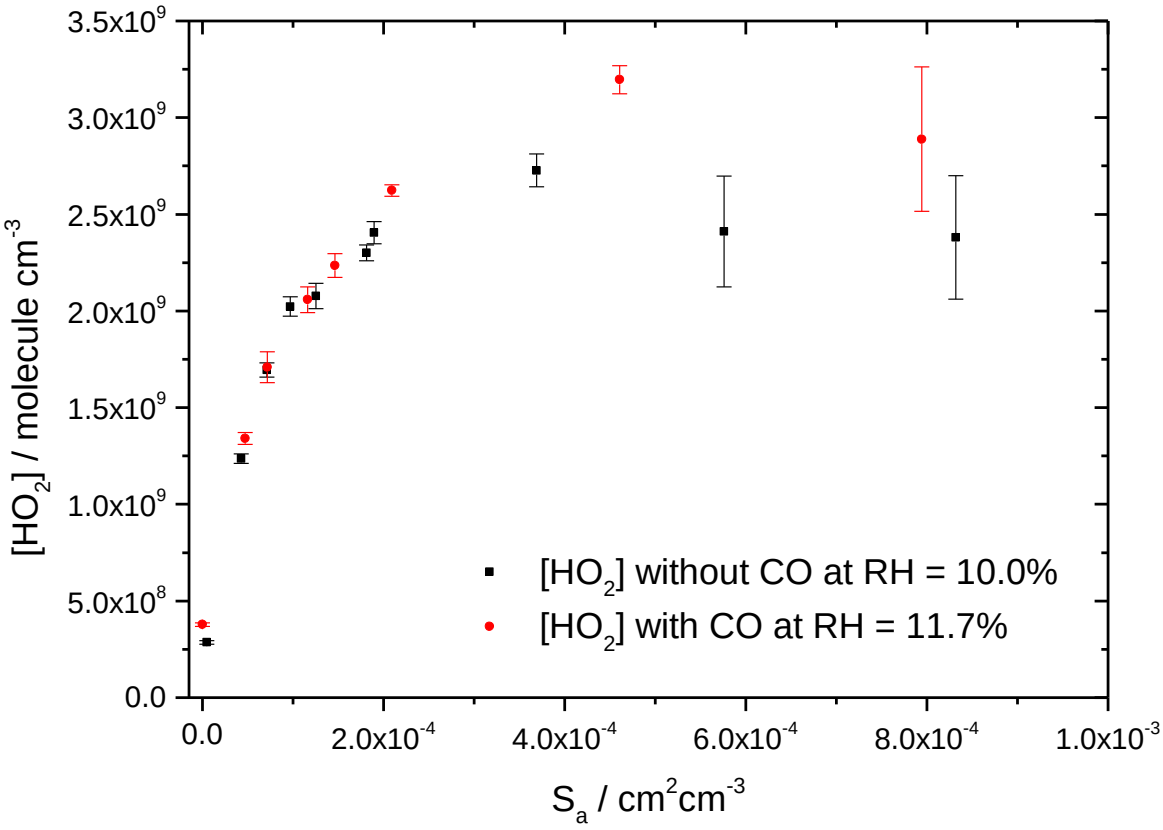

Figure 10. Gas-phase HO_2 produced by irradiated airborne TiO_2 nanoparticles at an irradiation time = 14 s as a function of S_a for $[O_2]$ = 5.9% without added CO (black squares, RH=10.0%) and with added CO (red circles, RH=11.7%).

OH is likely produced by the decomposition of H_2O_2 (R11) formed by HO_2 uptake, which is more prevalent at high $[HO_2]$ and S_a. The mechanism of H_2O_2 decomposition producing OH and the resulting OH reacting with H_2O_2, may explain the HO_2 observed by Yi et al. [4] (R11 and R13). Murikami et al. [9] directly observed gas-phase production of OH from irradiated TiO_2 surfaces. OH may be associated with H_2O_2 decomposition rather than from water oxidation, and a theoretical study [21] has shown that OH formed by water oxidation on anatase is likely to remain adsorbed on the surface rather than desorbing into the gas-phase and on rutile peroxy intermediates are formed rather than OH.

4. Discussion

Sources of HO_x radicals in the condensed phase that have been previously suggested include the uptake of OH and HO_2 from the gas-phase, followed by the formation of aqueous H_2O_2 and subsequent decomposition, as well as Fenton reactions of reduced metal ions and H_2O_2, and direct photolysis of H_2O_2, nitrite, nitrate, hydroperoxides, light-absorbing secondary aerosols and iron (III) complexes. [22] Although the formation of HO_2 from illuminated aerosols containing a photo-sensitizer (imidazole-2-carboxaldehyde) has been measured indirectly by converting gas-phase NO to NO_2, this study presents the first direct observations of HO_2 radicals generated on aerosol surfaces. These are the first observations of HO_2 production from illuminated TiO_2 surfaces in the presence of light and O_2, but without the presence of added H_2O_2, which was needed by Yi et al.[4] in order to see HO_2 from TiO_2 films. Unlike heterogeneous reactions involving surfaces or films, heterogeneous reactions involving airborne nanoparticles are not limited by diffusion of gas-phase reactants to the particle surface. To overcome diffusion limitations production from solid surfaces or thin film experiments are often performed at low pressure, however this will not favour adsorption of species with a high vapour pressure, such as water vapour. Yi et al. used pure forms of TiO_2 polymorphs which has been shown to enhance photocatalytic activity [14] rather than a blend, and surface or thin film experiments often take a number of minutes, so surface saturation and product accumulation may occur on the surface of the sample and could change its chemical characteristics.

The mechanism generating HO_2 on irradiated TiO_2 surfaces in the presence of O_2 is postulated to be (where V_{br}, O_{br} and OH_{br} are bridging vacancy, oxygen and hydroxyl groups):

$$TiO_2 + h\nu\ (\lambda < 388\ \text{nm}) \rightarrow TiO_2 + h^+_{VB} + e^-_{CB} \quad \text{(R1)}$$

$$H_2O + V_{br} + O_{br} \rightarrow 2OH_{br} \quad \text{(R21)}$$

$$OH_{br} + H_2O_{(g)} \leftrightharpoons OH_{br}\text{-}OH_{2\,(ad)} \quad \text{(R22)}$$

$$OH_{br}\text{-}\ OH_{2\,(ad)} + h^+ \rightarrow OH_{(ad)} + H^+_{(ad)} + OH_{br} \quad \text{(R23)}$$

$$Ti + O_{2(g)} \leftrightharpoons Ti\text{-}O_{2(ad)} \quad \text{(R24)}$$

$$Ti\text{-}O_{2(ad)} + e^-_{CB} \rightarrow Ti\text{-}O_2^-{}_{(ad)} \quad \text{(R25)}$$

$$Ti\text{-}O_2^-{}_{(ad)} + H^+_{(ad)} \rightarrow Ti\text{-}O_2H_{\,(ad)} \quad \text{(R26)}$$

$$Ti\text{-}O_2H_{\,(ad)} + h\nu \rightarrow Ti + HO_{2(g)} \quad \text{(R27)}$$

The reaction is initiated by the production of photogenerated electrons in the conduction band (e^-_{CB}) and holes within the valence band (h^+_{VB}), which can either recombine or reside in a trapped state or within

the respective band. O_2 is an effective electron scavenger forming either O_2^- or O_2^{2-}. A study of this process on TiO_2 (101) surfaces [23] showed that photogenerated e^- can exist on paramagnetic Ti^{3+} sites or delocalise within the conduction band. At room temperature, most photogenerated e^- remain stable within the conduction band rather than in trapped Ti^{3+} states, however at lower temperatures e^- can reside in these traps which could lead to a higher rate of O_2^- formation. That study observed the efficient production of long-lived O_2^-, with all photoexcited e^- being transferred to adsorbed O_2. It is likely that the mechanism for HO_2 production would therefore have to involve the reduction of adsorbed O_2 with e^-_{CB} forming adsorbed O_2^- (R25). O_2^- can then go on to react with a proton (R26) formed by the oxidation of adsorbed water via its reaction with a photogenerated h^+ (R23) located at bridging oxygen sites (O_{br}) for TiO_2 (110) and OH_{br} groups for TiO_2 (101) [24, 25] to form adsorbed HO_2. This mechanism highlights the contradictory role that water plays in the photocatalytic activity of TiO_2, on the one-hand producing active species on the surface of photocatalytically active TiO_2 available for reaction (R21) and, on the other hand, reducing the availability and effectiveness of active sites and therefore reducing adsorption of gas-phase species, as shown in Figures 8 and 9. It is also likely that desorption of HO_2 could be augmented by photodesorption (R27) as shown below in Figure 11:

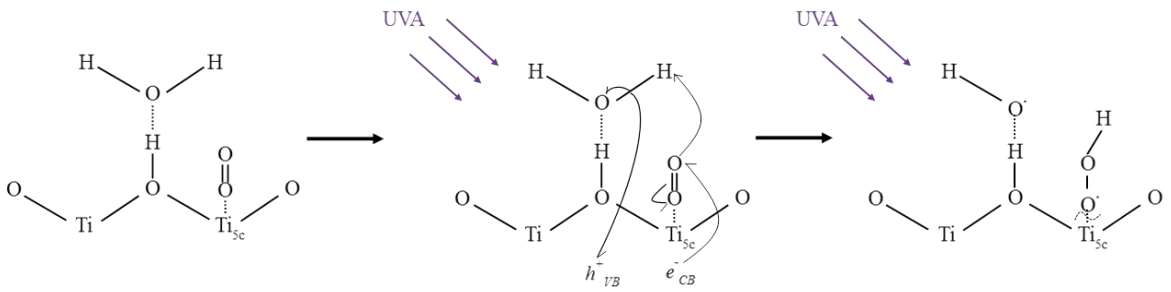

Figure 11. Mechanism for the production of gas-phase HO_2 from the surfaces of airborne TiO_2 nanoparticle. Ti_{5c} refers to fivefold coordinated Ti sites. h^+_{VB} refers to valence band holes and e^-_{CB} refers to conduction band electrons.

Adsorption of water vapour may inhibit the reaction by blocking adjacent O_2 adsorption sites reducing the effective surface area available and by reducing the O_2 adsorption binding energy and hence desorption lifetime. The value of K_{H2O} (obtained from Figure 8) shows that $K_{H2O} > K_{O2}$ suggesting that the H_2O adsorption enthalpy onto TiO_2 is larger than for O_2 adsorption and many more water molecules are adsorbed on the surface of the TiO_2 particle than O_2. This is consistent with studies that have shown TiO_2 surfaces become super-hydrophilic when irradiated with UV light. [26] Both K_{O2} and K_{H2O} decrease as RH was increased (Table 1) suggesting that the enthalpy of adsorption of both species is decreasing with RH. Bridging hydroxyl groups (OH_{br}), formed in R21 by dissociation of water at oxygen vacancy

defects in bridging sites (V_{br}) [27], provide an anchoring point for water molecules to adsorb onto TiO_2 surfaces forming OH_{br}-H_2O complexes (R22) which are acidic in character (i.e. OH_{br} groups act as H-donors). [27, 28] The enthalpy of water adsorption on these sites is ~ 70 kJ mol^{-1}. As RH is increased beyond 11% (RH for one monolayer of H_2O on TiO_2 [19]) a second monolayer of H_2O begins to form and H_2O binds to the OH_{br}-H_2O complexes, reducing their acidity and resulting in the water binding structure being more characteristic of bulk water [28] and a lowering of the H_2O adsorption enthalpy, and hence K_{H2O}. Density functional theory (DFT) calculations [29] have shown that O_2 adsorption onto TiO_2 (110, i.e. the rutile polymorph of TiO_2) surfaces is also entirely dependent on the presence of OH_{br} groups. These calculations show that the most stable configuration for O_2 adsorption is onto two adjacent fivefold coordinated Ti sites (Ti_{5c}) adjacent to an OH_{br} group with an adsorption enthalpy of ~ 77 kJ mol^{-1}. However, many other configurations have an adsorption enthalpy which is only slightly less (~ 58 kJ mol^{-1}), e.g. adsorption to a single Ti_{5c} site adjacent to an OH_{br} group. The calculations also show that the adsorption enthalpy of O_2 is dependent on the coverage of OH_{br}, with higher coverage of OH_{br} resulting in a higher enthalpy of adsorption and hence a longer adsorption lifetime for O_2. The distance between adsorbed O_2 and OH_{br} does not significantly affect the adsorption enthalpy, meaning OH_{br} exerts a long-range influence on O_2 adsorption via the donation of electrons to TiO_2 which delocalise amongst $Ti_{(5c)}$ atoms. Upon O_2 adsorption, there is a charge transfer from the $Ti_{(5c)}$ atoms to O_2 (R24), the magnitude of which determines the enthalpy of adsorption. The same mechanism was found for calculations of O_2 adsorption onto TiO_2 (101, anatase). [30] The decrease of K_{O2} with RH and the inhibiting effects of H_2O adsorption to the rate of HO_2 production observed in this work are likely associated with the formation of OH_{br}-H_2O complexes which inhibits the ability of OH_{br} groups to donate electron density to Ti_{5c} atoms thereby reducing the adsorption enthalpy of O_2 or alternatively, adsorption of H_2O blocks more favourable O_2 absorptions sites near OH_{br}. When the surface coverage of H_2O reaches ~1.6 monolayers (at RH = 40%) further adsorption of H_2O does not result in further inhibition of HO_2 formation (Figure 9). At sufficiently high RH large amounts of water may condense around the particle forming a liquid layer which may either block access of O_2 to all binding sites or any HO_2 formed remains solvated within the liquid layer.

A laboratory study investigating the photocatalytic performance of cement-based TiO_2-containing materials for reduction of gas-phase oxides of nitrogen (NO_x = NO + NO_2), [34] showed that upon illumination of the material within a standard flow reactor, concentrations of NO decreased from 100 ppm to 20 ppm and continued to fall over the period of a couple of hours until a steady-state concentration of 10 ppm was reached. During this time, gas-phase NO_2 was formed in the flow reactor and remained at a constant concentration of 10 ppm, with NO_2 potentially being produced via the gas-phase reaction of HO_2 generated at surfaces and NO. Furthermore, NO reduction showed a similar dependence to O_2 concentration and RH seen in this study.

5. Atmospheric Implications

TiO_2 surfaces are present in the troposphere, occurring naturally as a component of mineral dusts and artificially as building materials, such as self-cleaning glass or environmental catalysts, or from industrial sources, including the nanotechnology industry. TiO_2 nanoparticles are also a candidate for application within Solar-radiation Management (SRM) schemes to mitigate global warming due to their high refractive index and relative affordability. [18] It is proposed that TiO_2 nanoparticles could be injected into the dynamically stable lower stratosphere in order to back-scatter incoming solar-radiation to space resulting in a cooling effect to the Earth's climate. However, this SRM method carries significant risk, as the photocatalytic production of HO_2 radicals from TiO_2 surfaces may have the potential to perturb atmospheric chemistry, particularly in the lower stratosphere where HO_2 is involved in a HO_x catalytic cycle responsible for about 40% of O_3 depletion. [31] Also, heterogeneous processes are known to influence levels of active chlorine and NO_y partitioning in the stratosphere.

During the Saharan Mineral Dust Experiment **(**SAMUM-2) field campaign held at sea-level in the Cape Verde islands, typical dust concentrations ranged from 10 – 200 μg m^{-3} which correspond to surface areas of $2.2 \times 10^{-7} – 4.4 \times 10^{-6}$ cm^2 cm^{-3}, respectively. [32] In this same region, the proportion of TiO_2 in mineral dusts was measured to be 4.5% using energy dispersive X-ray spectroscopy, [33] from which we have estimated a range of effective surface areas for TiO_2. The measured values of k'_{prod} presented in section 3.1 above, which are the light flux and surface area independent rates of HO_2 production from TiO_2 aerosol surfaces, were used to calculate the HO_2 production rate from TiO_2 photocatalytic aerosol processes for a typical ambient sunlight flux (using the values at Weybourne, UK shown in Figure 2) and for a 20% mixing ratio of O_2 and RH ~20%. For the above range of TiO_2 surface areas, the rate of heterogeneous HO_2 production is estimated to range from $4.5 \times 10^4 – 1.6 \times 10^6$ molecule cm^{-3} s^{-1}. However, there is considerable uncertainty in this estimate owing in particular to difficulties in obtaining the absolute flux of the lamp within the flowtube. For comparison, the production rate of HO_2 from the gas-phase reaction between OH and CO, and assuming typical concentrations of [OH] = 2×10^6 molecule cm^{-3} (0.08 parts per trillion) and [CO] = 5×10^{12} molecule cm^{-3} (200 parts per billion), typical of the unpolluted troposphere, is 1.6×10^6 molecule cm^{-3} s^{-1}. Hence, during periods of significant loading of mineral dust the aerosol production mechanism could represent a significant source of HO_2 in the troposphere. However, further studies of HO_2 production from morphologies of TiO_2 typically found in mineral dust are required to provide a more accurate estrimate.

Considering the potential impact on stratospheric ozone chemistry of the production of HO_2 from TiO_2 aerosols used in SRM schemes, it is important to note that the HO_2 production rate is likely to demonstrate a strong temperature dependence, as adsorption is an exothermic process. Further studies which investigate the temperature dependence of HO_2 production from TiO_2 aerosols at stratospherically relevant partial pressures of H_2O and O_2 are required to further quantify any impact.

6. Conclusions

Upon illumination of airborne TiO_2 nanoparticles with near-UV light (~ 300 – 400 nm) in an aerosol flow tube in the presence of O_2 and water vapour, significant quantities of HO_2 was observed in the gas-phase. The dependence of HO_2 production on O_2 shows typical Langmuir adsorption behaviour suggesting O_2 is a reactant in the process generating HO_2. The addition of further H_2O vapour inhibits the production of HO_2 and reduces the adsorption equilibrium coefficient for both O_2 and H_2O, demonstrating the contradictory role of H_2O within the photocatalytic mechanism. Reduction of O_2 by photogenerated electrons is likely to be the initial step for HO_2 production followed by reaction of O_2^- with a proton produced via oxidation of adsorbed water with a photogenerated hole. The maximum rate coefficient (i.e. when $[O_2]$ is projected to atmospherically relevant levels) for production of gas-phase HO_2 normalised for surface area and light intensity was found to be $k'_{prod} = (3.64 \pm 0.04) \times 10^{-3}$ HO_2 molecule photon^{-1} at a RH of 8.7% for the 80% anatase and 20% rutile formulation of TiO_2 used here, although this decreased to $k'_{prod} = (1.97 \pm 0.03) \times 10^{-3}$ molecule photon^{-1} as the RH was increased to 22.1%. From surface areas of mineral dust observed at Cape Verde and assuming a TiO_2 fraction of 4.5%, the rate of heterogeneous production of HO_2 from TiO_2 surfaces was calculated to be in the range 5×10^4 – 1×10^6 molecule cm^{-3}s^{-1}, with the upper end of this range being similar to the rate of HO_2 production from the gas-phase reaction of OH with CO typical of unpolluted regions of the troposphere. Production of gas-phase OH radicals could only be observed for the largest concentrations of TiO_2 aerosols used, and are postulated to be formed from the photo-decomposition of H_2O_2 formed via self-reaction of HO_2 on the surfaces of the TiO_2 aerosols.

Acknowledgements

We are grateful to the Natural Environment Research Council for funding a studentship (DRM) and for funding the aerosol flow tube apparatus (grant number NE/F020651/1)). LKW, TI, PWS and and DEH are also grateful to the NERC funded National Centre for Atmospheric Science for ongoing support. We would also like to thank the two anonymous reviewers for helpful comments.

References

1. A. Fujishima and K. Honda, Nature, 1972, **238**, 37-38.
2. H. Chen, C. E. Nanayakkara and V. H. Grassian, Chem. Rev., 2012, **112**, 5919-5948.
3. J. A. Kent, Handbook of Industrial Chemistry and Biotechnology, Springer US2013.

4. J. Yi, C. Bahrini, C. Schoemaecker, C. Fittschen and W. Choi, J. Phys. Chem. C, 2012, **116**, 10090-10097.
5. A. Fujishima, X. Zhang and D. A. Tryk, Surface Science Reports, 2008, **63**, 515-582.
6. C. Bahrini, A. Parker, C. Schoemaecker and C. Fittschen, Appl. Catal. B-Environ., 2010, **99**, 413-419.
7. N. C. Lee and W. Y. Choi, J. Phys. Chem. B, 2002, **106**, 11818-11822.
8. T. Tatsuma, S. Tachibana and A. Fujishima, J. Phys. Chem. B, 2001, **105**, 6987-6992.
9. Y. Murakami, E. Kenji, A. Y. Nosaka and Y. Nosaka, J. Phys. Chem. B, 2006, **110**, 16808-16811.
10. G. Vincent, A. Aluculesei, A. Parker, C. Fittschen, O. Zahraa and P. M. Marquaire, J. Phys. Chem. C, 2008, **112**, 9115-9119.
11. J. Thiebaud, F. Thevenet and C. Fittschen, J. Phys. Chem. C, 2010, **114**, 3082-3088.
12. D. R. Moon, G. S. Taverna, C. Anduix-Canto, T. Ingham, M. P. Chipperfield, P. W. Seakins, M. T. Baeza-Romero and D. E. Heard, Atmos. Chem. Phys., 2018, **18**, 327-338.
13. D. E. Heard and M. J. Pilling, Chem. Rev., 2003, **103**, 5163-5198.
14. D. C. Hurum, A. G. Agrios, K. A. Gray, T. Rajh and M. C. Thurnauer, J. Phys. Chem. B, 2003, **107**, 4545-4549.
15. I. J. George, P. S. Matthews, L. K. Whalley, B. Brooks, A. Goddard, M. T. Baeza-Romero and D. E. Heard, Phys Chem Chem Phys, 2013, **15**, 12829-12845.
16. F. A. F. Winiberg, S. C. Smith, I. Bejan, C. A. Brumby, T. Ingham, T. L. Malkin, S. C. Orr, D. E. Heard and P. W. Seakins, Atmos. Meas. Tech., 2015, **8**, 523-540.
17. J. C. Ianni, in Computational Fluid and Solid Mechanics 2003, Elsevier Science Ltd, Oxford 2003, pp. 1368-1372.
18. F. D. Pope, P. Braesicke, R. G. Grainger, M. Kalberer, I. M. Watson, P. J. Davidson and R. A. Cox, Nat. Clim. Chang., 2012, **2**, 713-719.
19. A. L. Goodman, E. T. Bernard and V. H. Grassian, Journal of Physical Chemistry A, 2001, **105**, 6443-6457.
20. L.-L. Tan, W.-J. Ong, S.-P. Chai and A. R. Mohamed, Chemical Engineering Journal, 2017, **308**, 248-255.
21. R. Li, Y. Weng, X. Zhou, X. Wang, Y. Mi, R. Chong, H. Han and C. Li, Energy & Environmental Science, 2015, **8**, 2377-2382.
22. L. González Palacios, P. Corral Arroyo, K. Z. Aregahegn, S. S. Steimer, T. Bartels-Rausch, B. Nozière, C. George, M. Ammann and R. Volkamer, Atmos. Chem. Phys., 2016, **16**, 11823-11836.
23. T. Berger, M. Sterrer, O. Diwald, E. Knözinger, D. Panayotov, T. L. Thompson and J. T. Yates, The Journal of Physical Chemistry B, 2005, **109**, 6061-6068.
24. Y. Ji, B. Wang and Y. Luo, The Journal of Physical Chemistry C, 2014, **118**, 21457-21462.
25. Y. Ji, B. Wang and Y. Luo, The Journal of Physical Chemistry C, 2014, **118**, 1027-1034.
26. L. Sirghi and Y. Hatanaka, Surface Science, 2003, **530**, L323-L327.
27. S. Yamamoto, H. Bluhm, K. Andersson, G. Ketteler, H. Ogasawara, M. Salmeron and A. Nilsson, J. Phys.-Condes. Matter, 2008, **20**, 14.
28. G. Ketteler, S. Yamamoto, H. Bluhm, K. Andersson, D. E. Starr, D. F. Ogletree, H. Ogasawara, A. Nilsson and M. Salmeron, J. Phys. Chem. C, 2007, **111**, 8278-8282.
29. L. M. Liu, B. McAllister, H. Q. Ye and P. Hu, Journal of the American Chemical Society, 2006, **128**, 4017-4022.
30. Y.-F. Li, U. Aschauer, J. Chen and A. Selloni, Accounts of Chemical Research, 2014, **47**, 3361-3368.
31. P. O. Wennberg, Cohen, R. C., Stimpfle, R. M., Koplow, J. P., Anderson, J. G., Salawitch, R. J., Fahey, D. W., Woodbridge, E. L., Keim, E. R., Gao, R. S., Webster, C. R., May, R. D., Toohey, D. W., Avallone, L. M., Proffitt, M. H., Loewenstein, M., Podolske, J. R., Chan, K. R., Wofsy, S. C., Science, 1994, **266**, 398-404.
32. A. Schladitz, T. Müller, A. Nowak, K. Kandler, K. Lieke, A. Massling and A. Wiedensohler, Tellus B: Chemical and Physical Meteorology, 2011, **63**, 531-548.
33. F. Hanisch and J. N. Crowley, Atmos. Chem. Phys., 2003, **3**, 119-130.

34. F. Mothes, S. Ifang, M. Gallus, B. Golly, A. Boréave, R. Kurtenbach, J. Kleffmann, C. George and H. Herrmann, Applied Catalysis B: Environmental, 2018, **231**, 161-172.